IOPscience iopscience.iop.org

Home Search Collections Journals About Contact us My IOPscience

Colour centre production in yttria-stabilized zirconia by swift charged particle irradiations

This article has been downloaded from IOPscience. Please scroll down to see the full text article.

2004 J. Phys.: Condens. Matter 16 3957

(http://iopscience.iop.org/0953-8984/16/23/014)

View the table of contents for this issue, or go to the journal homepage for more

Download details:
IP Address: 129.252.86.83
The article was downloaded on 27/05/2010 at 15:19

Please note that terms and conditions apply.

INSTITUTE OF PHYSICS PUBLISHING JOURNAL OF PHYSICS: CONDENSED MATTER

J. Phys.: Condens. Matter **16** (2004) 3957–3971 PII: S0953-8984(04)76964-7

Colour centre production in yttria-stabilized zirconia by swift charged particle irradiations

Jean-Marc Costantini[1], François Beuneu[2], Didier Gourier[3], Christina Trautmann[4], Georges Calas[5] and Marcel Toulemonde[6]

[1] Commissariat à l'Énergie Atomique/Saclay, DMN/SRMA, F-91191 Gif-sur-Yvette Cedex, France
[2] Laboratoire des Solides Irradiés, CEA-CNRS, École Polytechnique, F-91128 Palaiseau Cedex, France
[3] Laboratoire de Chimie Appliquée de l'Etat Solide, UMR-CNRS 7574, Ecole Nationale Supérieure de Chimie de Paris, 11 Rue Pierre et Marie Curie, F-75231 Paris Cedex 05, France
[4] Gesellschaft für Schwerionenforschung, Planckstrasse 1, D-64291, Darmstadt, Germany
[5] Laboratoire de Minéralogie-Cristallographie, UMR-CNRS 7590, Université Pierre-et-Marie Curie, 4 place Jussieu, F-75252, Paris Cedex 5, France
[6] Centre Interdisciplinaire de Recherches Ions Laser, CEA-CNRS-ISMRA, Rue Claude Bloch, BP 5133, F-14070 Caen Cedex, France

Received 26 February 2004
Published 28 May 2004
Online at stacks.iop.org/JPhysCM/16/3957
DOI: 10.1088/0953-8984/16/23/014

Abstract

We have studied the colour centre production by swift electron and heavy ion irradiations of yttria-stabilized zirconia (YSZ), i.e. ZrO_2:Y with 9.5 mol% Y_2O_3. For this purpose, we performed irradiations of ⟨100⟩- or ⟨110⟩-oriented YSZ single crystals with 2.5 MeV electrons, 145 MeV ^{13}C, 180 MeV ^{32}S, 200 MeV ^{58}Ni, 230 MeV ^{79}Br, 120 MeV ^{127}I, 200 MeV ^{127}I, 200 MeV ^{197}Au, and 2.6 GeV ^{238}U ions. X-band electron paramagnetic resonance (EPR) and UV–visible optical absorption measurements were used to monitor the point defect formation. The EPR line saturations were measured between 6 and 150 K, in order to obtain the spin–lattice relaxation time (T_1). Electron and ion beams produce the same two colour centres: (i) the first one is identified as an F^+-type centre (singly ionized oxygen vacancy) with an axial ⟨100⟩ symmetry, a small g-factor anisotropy ($g_\perp = 1.972$ and $g_\parallel = 1.996$) and long T_1 values, (ii) the second one is similar to the well known T-centre (Zr^{3+} in a trigonal oxygen environment) with an axial ⟨111⟩ symmetry and a large g-factor anisotropy ($g_\perp = 1.855$ and $g_\parallel = 1.986$), which is also produced by photon irradiations. A broad optical absorption band centred at a wavelength near 500 nm is observed with an absorption coefficient proportional to the volume density of the F^+-type centre deduced from the room temperature EPR spectra. Since no change of this band occurs between 10 and 300 K, it indicates that the electron–phonon coupling of this colour centre must be strong, in agreement with an F^+-type centre. Owing to the axial ⟨100⟩ symmetry and lack of hyperfine structure of the EPR lines of this defect, it is suggested that the first coordination shell must

 © 2004 IOP Publishing Ltd Printed in the UK

contain one native oxygen vacancy. The plots of the volume density of this centre versus fluence are on the whole rescaled as functions of the number of displacements per atom induced by elastic collisions.

(Some figures in this article are in colour only in the electronic version)

1. Introduction

Zirconium dioxide or zirconia (ZrO_2) is one of the most studied refractory materials suitable as a host for actinide transmutation [1]. The stability of the fully stabilized cubic phase under heavy ion or fast neutron irradiations has been extensively investigated [2]. It is established that heavy ion irradiations do not induce amorphization in cubic zirconia due to intrinsic defects produced either by ballistic processes (even at 120 K) or by electronic excitations up to high fluences [2]. However, the point defects induced by swift charged particles are still not well known compared to other matrix candidates such as for instance magnesia (MgO).

On the basis of electron paramagnetic resonance (EPR) spectroscopy data, we have shown in earlier studies that two different paramagnetic centres are produced by 2.5 MeV electron irradiations of yttria-stabilized zirconia (YSZ) single crystals at room temperature (RT) [3, 4]:

(i) the first one (hereafter referred to as the A-centre) has an axial ⟨100⟩ symmetry and g-factor values smaller than the free electron value (this centre is different from the orthorhombic oxygen hole centre (OHC) induced by x-ray irradiation at liquid nitrogen temperature, which is not stable at RT [5]);
(ii) the second one (hereafter referred to as the B-centre) has an axial ⟨111⟩ symmetry and is similar to the T-centre (Zr^{3+}) induced by photon irradiations, stable at RT [5–7].

We found that the stability of both defects increases with increasing electron fluence [4], and that heavy ion (2.6 GeV U) irradiations of reduced vacuum-annealed samples produce the same defects as the 2.5 MeV electron beam [3]. The aim of the present study was then to record new EPR and optical absorption data using different charged particles over a wide range of stopping power in order to monitor the production of point defects in this material, and elucidate the mechanisms of defect creation. We show that the A-centre is likely to be an F^+-type centre (singly ionized oxygen vacancy) induced by the elastic collisions. The defect production kinetics are scaled versus the number of displacements per atom. The B-centre is a Zr^{3+} ion associated with two oxygen vacancies which is most probably induced by the electronic excitations.

2. Experimental details

For this study we used YSZ single crystals, i.e. ZrO_2:Y (with 9.5 mol% Y_2O_3), with the ⟨100⟩ or ⟨110⟩ orientations and thickness of 100 or 500 μm, provided by Crystal-GmbH (Berlin, Germany). Two kinds of sample were used: as-received (AR) and reduced (R) ones. The AR-samples with formula $Zr_{0.8}Y_{0.2}O_{1.9}V_{O0.1}$ contain around 10 at.% oxygen vacancies with a 2+ charge state induced by charge compensation of Y^{3+} substituted for Zr^{4+} ions. The R-samples were obtained by thermal annealing in vacuum for 24 h at 1100 °C. By this treatment, Zr^{3+} ions (C-centres) are produced by a charge-compensating effect of the extra oxygen vacancies retained at RT from the high temperature [5, 8].

EPR measurements were carried out using a computerized Bruker ER 200D X-band spectrometer operating at 9.6 GHz. The estimated uncertainty on the g-factor values is ± 0.001

with a NMR probe. Measurements were also performed between 4.2 and 300 K in an Oxford ESR 900 continuous liquid He-flow cryostat. UV–visible optical absorption measurements were achieved between 10 and 300 K with a Cary-5 spectrometer equipped with an Oxford cryo-cooler.

The 2.5 MeV electron irradiations of 500 μm thick AR-samples were performed under helium gas at around 310 K and flux $\phi \approx 10^{14}$ cm^{-2} s^{-1}. The electrons were transmitted through the samples. For the sake of comparison, ⟨100⟩ and ⟨110⟩ AR-samples were x-ray irradiated at room temperature with Cu Kα radiation for 190 h over a depth of 18 μm, corresponding to a 90% attenuation of the x-ray beam intensity.

The heavy ion irradiations (table 1) were carried out at GANIL in Caen for the irradiation with the C ions, at the VIVITRON in Strasbourg for the S, Ni, Br, I, and Au ions, and at GSI/UNILAC in Darmstadt for the U ions. The S, Ni, Br, I, Au, and U ions were implanted in the 500 μm thick samples. Carbon ions were implanted in 500 μm thick samples either at 145 or at 100 MeV through a 150 μm thick Al degrader foil. The 145 MeV C ions were also transmitted through 100 μm thick samples. Irradiations were performed under high vacuum with low particle fluxes ($\phi \approx 10^{8}$–10^{10} cm^{-2} s^{-1}) in order to prevent sample heating. The temperature during irradiations was thus near RT, except for the carbon beams which were applied at 77 K. The irradiation parameters such as range and stopping power, as computed with the TRIM96 code [9] for ions and with the ESTAR code [10] for electrons, are listed in table 1.

Subsequent to the irradiation with the 200 MeV I ions at a fluence of 3×10^{13} cm^{-2}, the 100 μm thick samples exhibited a strong curvature, whereas the 500 μm thick ⟨100⟩ samples broke along the ⟨110⟩ axis in the sample plane. Similarly, after irradiating with the 2.6 GeV U ions at a fluence of 9×10^{11} cm^{-2} a volume expansion near 0.2% was measured by surface profilometry [3], while at 1×10^{13} cm^{-2} the 500 μm thick ⟨100⟩ samples broke along ⟨110⟩.

3. Defect characterization

3.1. EPR data

The AR-samples were colourless, transparent, and with a weak EPR line at $g \approx 4$ attributed to Fe^{3+} impurities. No line due to the oxygen vacancies was seen. The ⟨100⟩ R-samples were yellow, and with a broad EPR line at $g = 1.890$ detectable at room temperature with the applied magnetic field $B \parallel \langle 100 \rangle$. This line was previously attributed to a point defect (C-centre) made of one Zr^{3+} ion associated with one oxygen vacancy [5].

Figure 1(a) shows the RT EPR spectra with $B \parallel \langle 100 \rangle$ in the case of 145 MeV carbon ions implanted in 500 μm thick ⟨100⟩ AR-samples and 145 MeV carbon ions transmitted through 100 μm thick ⟨100⟩ AR-samples at the same fluence of 9.3×10^{14} cm^{-2}. These two spectra are almost identical and exhibit three main lines: i.e. a narrow line at $g = 1.998$ (line 1), a broad signal at $g = 1.973$ (line 2) and a very broad one at $g = 1.890$ (line 3). The same three lines with different intensities are found in the spectra with $B \parallel \langle 100 \rangle$ of S-, Ni-, Br-, I-, and Au-ion-implanted or 2.5 MeV electron-irradiated ⟨100⟩ AR-samples (figure 1(b)). Yet, line 3 intensity is much weaker with the ions than with electrons, even at the larger fluences. No EPR signal is found at RT up to a fluence of 1×10^{13} cm^{-2} in U-ion-implanted AR-samples. However, the same three lines are observed at RT in the U-ion-implanted R-samples at a low fluence (1×10^{11} cm^{-2}).

All these lines are simulated with Lorentzian curves and integrated intensities (I) are deduced from a least-squares fitting procedure. The number of paramagnetic centres is then deduced from a calibration using a copper sulfate reference sample. Line 3 intensity follows

Table 1. Data on the A-centre generation in YSZ single crystals ($\rho = 5.8$ g cm^{-3}) (AR, as received; R, reduced vacuum annealed) with the ⟨100⟩ or ⟨110⟩ orientations and thickness h after charged particle irradiations with energy E, mean projected range R_p, and mean electronic stopping power S_e: number of displaced atoms per incident particle (N_d), asymptotic value of the volume density (N_∞), saturation cross section deduced from EPR data (σ) and from optical absorption data (σ_o), elastic–collision production yield (Y), and radiochemical yield (G).

Particle	Sample state	Orientation	E (MeV)	R_p (μm)	S_e (keV nm^{-1})	h (μm)	N_d	N_∞ (cm^{-3})	σ (cm^2)	σ_o (cm^2)	Y (%)	G (100 eV^{-1})
e^-	AR	⟨100⟩	2.5	3×10^3	8×10^{-4}	500	0.13	1.6×10^{17}	3.2×10^{-19}		1.9	6.4×10^{-7}
^{13}C	AR	⟨100⟩	145	160	0.9	500	965	8.4×10^{17}	2.5×10^{-15}		3.5	2.3×10^{-5}
	R	⟨100⟩						7.2×10^{17}	9.7×10^{-15}		11	
^{13}C	AR	⟨100⟩	100	80	0.8	500	850	1.8×10^{18}	1.3×10^{-15}		2.2	1.9×10^{-5}
	R	⟨100⟩						1.8×10^{18}	1.3×10^{-15}		2.2	
^{13}C	AR	⟨100⟩	145	160	0.6	100	150	2.1×10^{17}	2.0×10^{-15}		2.8	7.0×10^{-6}
	R	⟨100⟩						6.1×10^{17}	2.1×10^{-15}		8.5	
^{32}S	AR	⟨100⟩	180	30	6	500	4.1×10^3	2.7×10^{17}	9.6×10^{-14}		2.0	4.3×10^{-5}
^{58}Ni	AR	⟨100⟩	200	16	12.5	500	1.0×10^4	2.3×10^{18}	7.7×10^{-14}	1.7×10^{-13}	2.8	1.4×10^{-4}
	AR	⟨110⟩						3.3×10^{17}	1.2×10^{-13}		0.6	
^{79}Br	AR	⟨110⟩	230	15	15.3	500	1.7×10^4	1.3×10^{18}	1.4×10^{-13}	3.7×10^{-13}	1.6	1.2×10^{-4}
^{127}I	AR	⟨110⟩	120	9	13.3	500	3.3×10^4	1.2×10^{18}	7.5×10^{-13}	9.3×10^{-13}	2.4	6.7×10^{-4}
^{127}I	AR	⟨100⟩	200	12	16.7	500	3.2×10^4	2.6×10^{18}	4.3×10^{-13}		4.2	6.7×10^{-4}
	R	⟨100⟩						6.4×10^{18}	2.4×10^{-13}		5.8	
^{197}Au	AR	⟨100⟩	200	10	20	500	5.3×10^4	2.4×10^{18}	9.0×10^{-13}	1.0×10^{-12}	4.1	1.1×10^{-3}
	AR	⟨110⟩						7.7×10^{17}	1.7×10^{-12}		2.5	

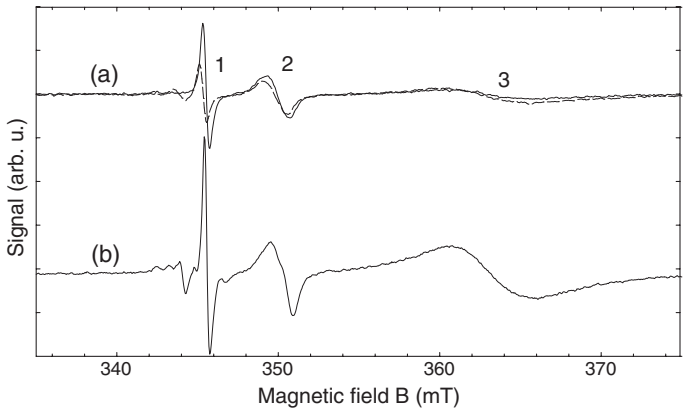

Figure 1. Room temperature EPR spectrum with applied magnetic field $B \parallel \langle 100 \rangle$ of as-received $\langle 100 \rangle$ YSZ single crystals: (a) 145 MeV C ions implanted in the 500 μm thick sample (solid) and 145 MeV C ions transmitted through the 100 μm thick sample (dashed) at a fluence of 9.3×10^{14} cm^{-2}; (b) 2.5 MeV electron irradiation at 2.9×10^{18} cm^{-2}.

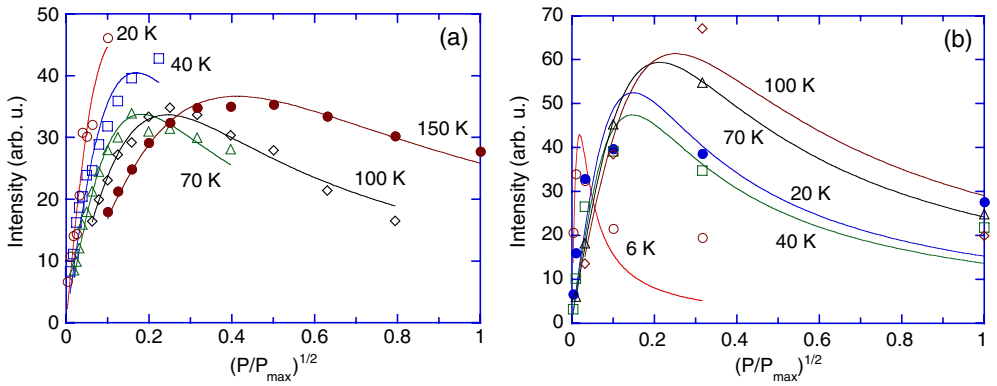

Figure 2. Saturation behaviour of the integrated intensity of line 1 versus reduced microwave field $H_1/H_{1\,\mathrm{max}} = (P/P_{\mathrm{max}})^{1/2}$, for (a) 2.5 MeV electron-irradiated (2.9×10^{18} cm^{-2}) as-received $\langle 100 \rangle$ YSZ single crystal at 20 K (open circles), 40 K (open squares), 70 K (open triangles), 100 K (open diamonds), and 150 K (full circles); (b) 200 MeV I-ion-irradiated (1.0×10^{13} cm^{-2}) as-received $\langle 100 \rangle$ YSZ single crystal at 6 K (open circles), 20 K (full circles), 40 K (open squares), 70 K (open triangles), and 100 K (open diamonds). Solid lines are least-squares-fitted curves using equation (1).

a Curie law versus temperature down to about 20 K for both electron- and ion-irradiated samples. In contrast, line 1 intensity exhibits apparent deviations from the Curie law below 150 K at rather low radio-frequency power (P) either for electron- or ion-irradiated samples. Line saturation was studied by plotting I versus $(P/P_{\mathrm{max}})^{1/2} = H_1/H_{1\,\mathrm{max}}$, where H_1 is the microwave field in the cavity. For both electron- and ion-irradiated samples, line 1 exhibits a homogeneous saturation below 150 K (figures 2(a) and (b)). No saturation is observed for line 2, while an inhomogeneous saturation behaviour is found for line 3, i.e. the intensity does not decrease at high microwave power.

The spin–lattice (T_1) and spin–spin (T_2) relaxation times are determined for electron or I ion irradiations by fitting the line intensity (I) versus H_1 with the following law for

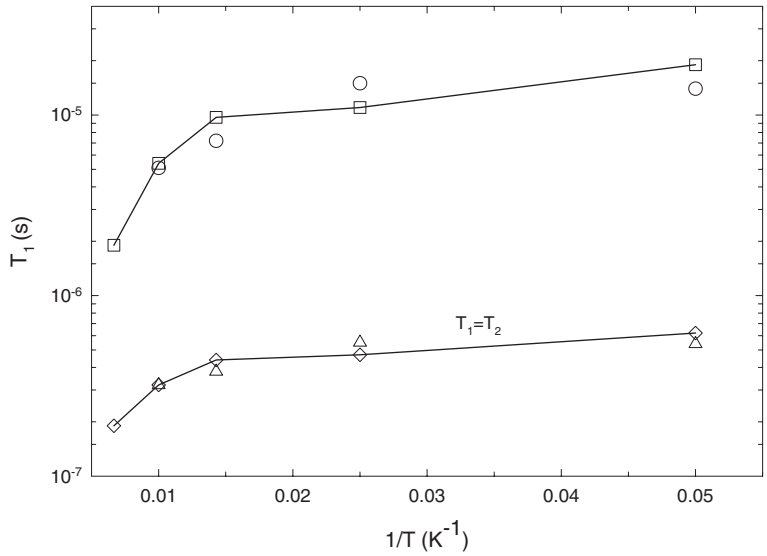

Figure 3. Spin–lattice relaxation time (T_1) versus reciprocal temperature deduced from the saturation curves (figure 2) with a spin–spin relaxation time $T_2 = 2 \times 10^{-8}$ s for the A-centre created by 2.5 MeV electron irradiation at 2.9×10^{18} cm^{-2} (open squares) and 200 MeV I ion irradiation at 1×10^{13} cm^{-2} (open circles) of ⟨100⟩ as-received YSZ single crystals; calculated values in the case of the extreme narrowing regime ($T_1 = T_2$) for electron (open diamonds) and iodine ion (open triangles) irradiations. (Lines are guides for the eyes.)

homogeneous saturation [11]:

$$I = K H_1/(1 + \gamma_e^2 H_1^2 T_1 T_2) \tag{1}$$

where K is a constant and γ_e the electronic gyromagnetic ratio. Hence $T_1 T_2$ is obtained from least-squares fitting, and T_1 is obtained by using a value of T_2 deduced from the half-width at half maximum of the Lorentzian line ΔB_{12} by the equation $T_2 = (\gamma_e \Delta B_{12})^{-1}$. When temperature decreases, T_1 increases dramatically, whereas T_2 remains almost constant ($T_2 \approx 2 \times 10^{-8}$ s). An alternative situation corresponds to the extreme line narrowing by rapid exchange interaction, with $T_1 = T_2 = \sqrt{T_1 T_2}$, that gives shorter relaxation times. In both cases, a very good agreement is found between electron and ion irradiation data (figure 3). However, it is important to note that the low spin density (see below), corresponding to 5–50 ppm, precludes a narrowing effect by rapid exchange interactions, unless we assume that the paramagnetic defects are inhomogeneously distributed, with local concentrations which are much higher than the average concentration.

Room temperature EPR spectra were recorded at various angles between B and the ⟨100⟩ direction in a {100} plane for a C-ion-implanted ⟨100⟩ AR-sample at 9.3×10^{14} cm^{-2} (figure 4). The same g-factor anisotropy is found as for 2.5 MeV electron-irradiated samples [4]. These data are confirmed by recording the spectra at various angles between B and ⟨100⟩ in a {100} plane for a S-ion-implanted ⟨110⟩ AR-sample at 3×10^{13} cm^{-2}. We thus conclude that lines 1 and 2 correspond to one and the same centre as that of electron irradiations (hereafter referred to as the A-centre), with an axial ⟨100⟩ symmetry and g-tensor principal values $g_\perp = 1.972$ and $g_\parallel = 1.996$ at RT, measured with the NMR probe in the case of S ion implantation, and $g_\perp = 1.96(9)$ and $g_\parallel = 1.99(4)$ without the NMR probe in the case of C ion implantation. These values are in good agreement with new measurements on a 2.5 MeV electron-irradiated AR sample at 2.9×10^{18} cm^{-2}, giving $g_\perp = 1.96(7)$ and $g_\parallel = 1.99(3)$, without the NMR probe.

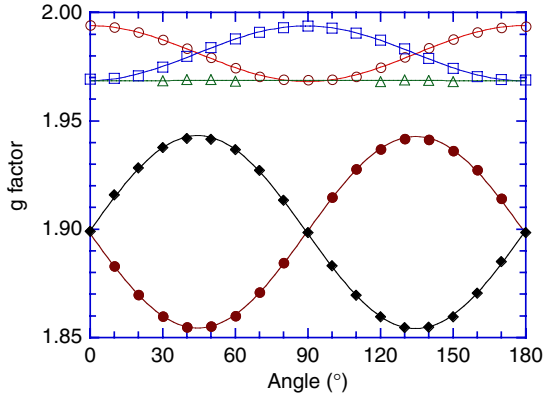

Figure 4. Room temperature g-factor versus the angle between the applied magnetic field B and ⟨100⟩ in a {100} plane for as-received ⟨100⟩ YSZ single crystals implanted with 145 MeV carbon ions (9.3×10^{14} cm^{-2}). Open symbols correspond to the A-centre (lines 1 and 2 of figure 1) and full ones to the B-centre (line 3 of figure 1). Solid lines are least-squares-fitted curves.

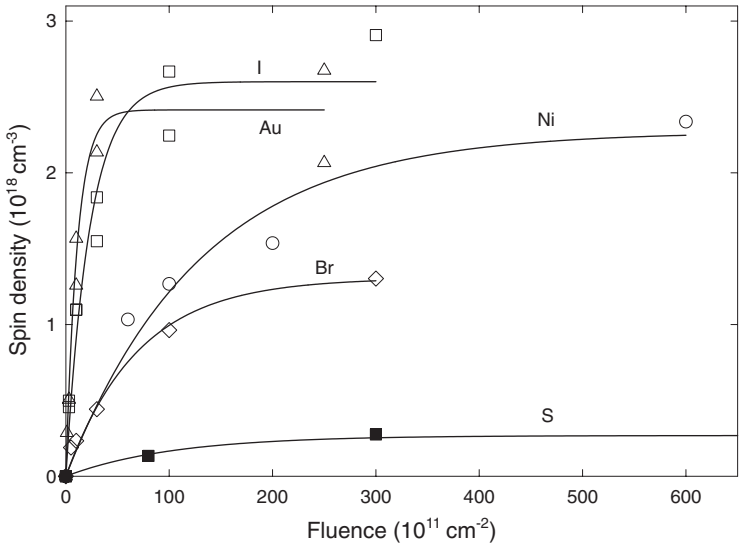

Figure 5. Volume density of A-centre versus ion fluence for as-received ⟨100⟩ YSZ single crystals implanted with 180 MeV S (full squares), 200 MeV Ni (open circles), 200 MeV I (open squares), and 200 MeV Au ions (open triangles), and as-received ⟨110⟩ YSZ single crystals implanted with 230 MeV Br ions (open diamonds). Solid lines are least-squares-fitted curves using equation (2).

Line 3 corresponds to a different centre with an axial ⟨111⟩ symmetry with g-factor principal values $g_\perp = 1.855$ and $g_\parallel = 1.986$ at RT in the case of C ion implantation, nearly identical to the T-centre found with the 2.5 MeV electron irradiations [4]. New measurements of the latter centre for electron irradiation (at 2.9×10^{18} cm^{-2}) give $g_\perp = 1.859$ and $g_\parallel = 1.989$ with the NMR probe at RT. In the case of x-ray irradiated ⟨100⟩ AR-samples, a similar centre is found at RT with a broad line at $g = 1.904$ for $B \parallel \langle 100 \rangle$, and the same g-factor anisotropy.

The volume densities (N) of A-centres at RT are plotted versus ion and electron fluence for ⟨100⟩ AR samples (figures 5 and 6) and R-samples. N is obtained by dividing the number of centres per unit surface of the irradiated sample by the mean projected range (R_p) for the

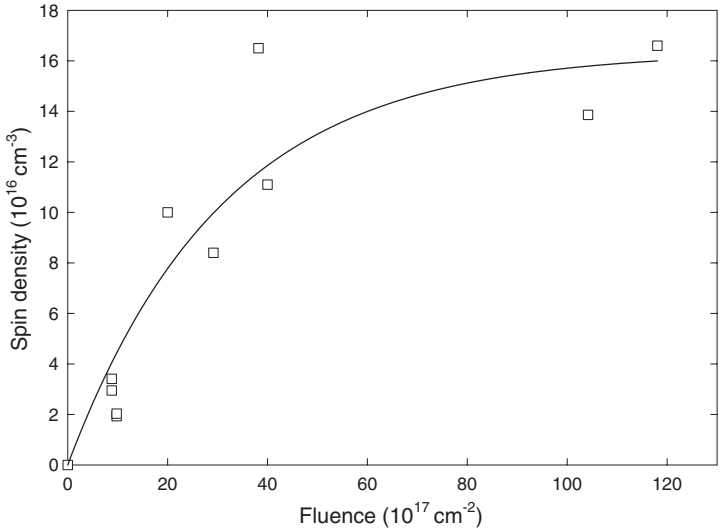

Figure 6. Volume density of A-centre versus fluence for 2.5 MeV electron-irradiated as-received ⟨100⟩ YSZ single crystals. The solid line is a least-squares-fitted curve using equation (2).

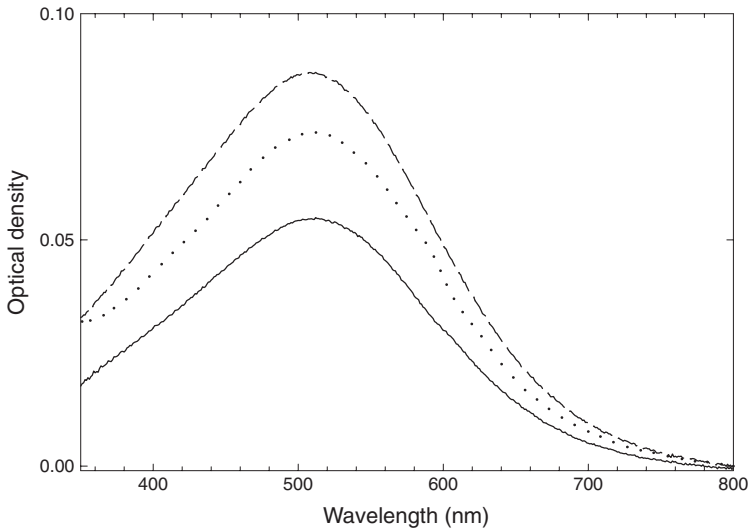

Figure 7. Room temperature UV–visible spectra of 200 MeV Au-ion-implanted as-received ⟨100⟩ YSZ single crystals at increasing fluences, after subtraction of the virgin sample spectrum and setting the OD at 800 nm to zero in order to correct for the sample reflectance: 1.0×10^{12} (solid) 3.0×10^{12} (dotted), 2.5×10^{13} cm^{-2} (dashed).

implanted ions or by the sample thickness (h) for transmitted ions and electrons. Note that the B-centre intensities could not be obtained reliably at RT for most ion irradiations, even at large fluences, due to the weak EPR signal.

3.2. Optical absorption data

Figure 7 shows the RT absorption spectra of Au-ion-implanted ⟨100⟩ AR-samples at increasing fluences in the 350–800 nm wavelength range. The virgin sample spectrum shows a

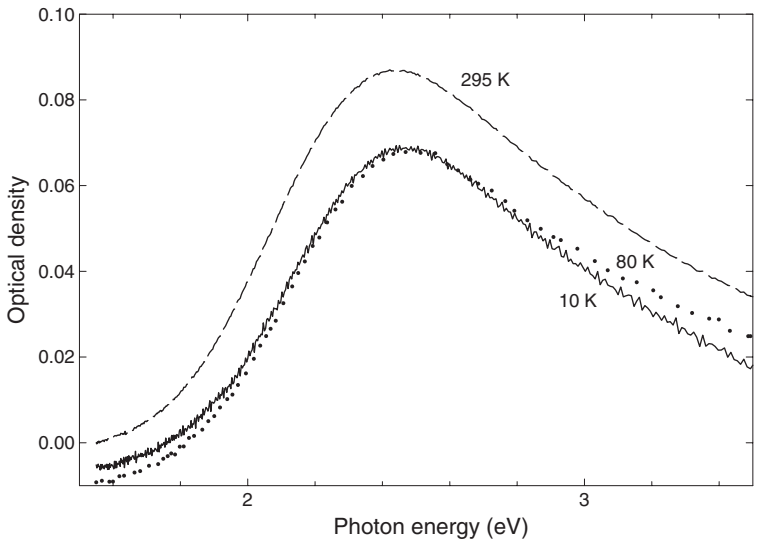

Figure 8. Low-temperature UV–visible spectra of 200 MeV Au-ion-implanted as-received ⟨100⟩ YSZ at 2.5×10^{13} cm^{-2} (after subtraction of the virgin sample spectrum): 10 K (solid), 80 K (dotted), 295 K (dashed) (spectra are shifted for the sake of clarity).

fundamental absorption edge at around 300 nm, corresponding to a bandgap near 4.1 eV, in agreement with the accepted value of 4.23 eV [12]. No other band is observed in the measured range. The latter reference spectrum was subtracted from the implanted sample spectra and the optical density (OD) was then set to zero at 800 nm in order to correct for the sample surface reflectance (R). With a refractive index $n = 2.1585$ [13], it yields $R = (n-1)^2/(n+1)^2 = 13.4\%$ at each zirconia/air interface. Thus the transmittance through the samples is $T = 73.1\%$ and $\mathrm{OD} = -\ln T = 0.136$, in agreement with an OD around 0.12 at 800 nm for the reference samples. Similar features are found in the case of Ni-ion-implanted ⟨100⟩ AR-samples and Br or I-ion-implanted ⟨110⟩ AR-samples: i.e. a purple colouration corresponding to a very broad absorption band with a maximum near 2.5 eV (figure 8). No clear modification of the band shape and intensity is seen down to 10 K (figure 8). U-ion-implanted AR-samples remain colourless, in agreement with the absence of EPR lines at RT. The maximum OD at 500 nm is plotted versus fluence (figure 9). The absorption coefficient at 500 nm ($\alpha = 2.3\mathrm{OD}/R_\mathrm{p}$) is also plotted versus the volume density of A-centres for Ni, Br, I, and Au ions at various fluences (figure 10).

4. Analysis of defect production

4.1. Defect production kinetics

Least-squares fits of the defect densities per irradiated sample volume (N) versus fluence (ϕt) (figures 5 and 6) were performed with the following law:

$$N = N_\infty[1 - \exp(-\sigma\phi t)] \tag{2}$$

where N_∞ is the asymptotic value of the defect volume density, σ a phenomenological cross section for saturation in the particle track, ϕ the particle flux, and t the irradiation time. At low fluence, the linear approximation of equation (2) gives

$$N = N_\infty \sigma \phi t. \tag{3}$$

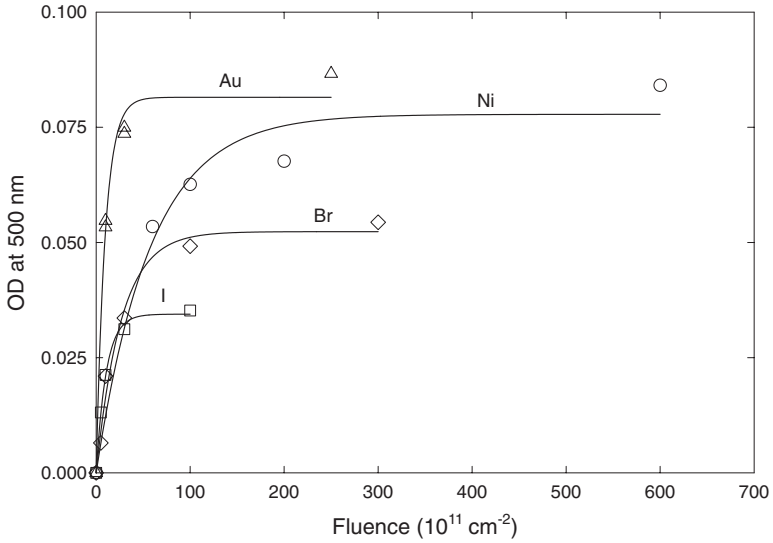

Figure 9. Maximum optical density (at 500 nm) versus fluence for as-received ⟨100⟩ YSZ single crystals implanted with 200 MeV Ni (open circles) and 200 MeV Au ions (open triangles), and as-received ⟨110⟩ YSZ single crystals implanted with 230 MeV Br (open diamonds) and 120 MeV I ions (open squares). Solid lines are least-squares-fitted curves using equation (2).

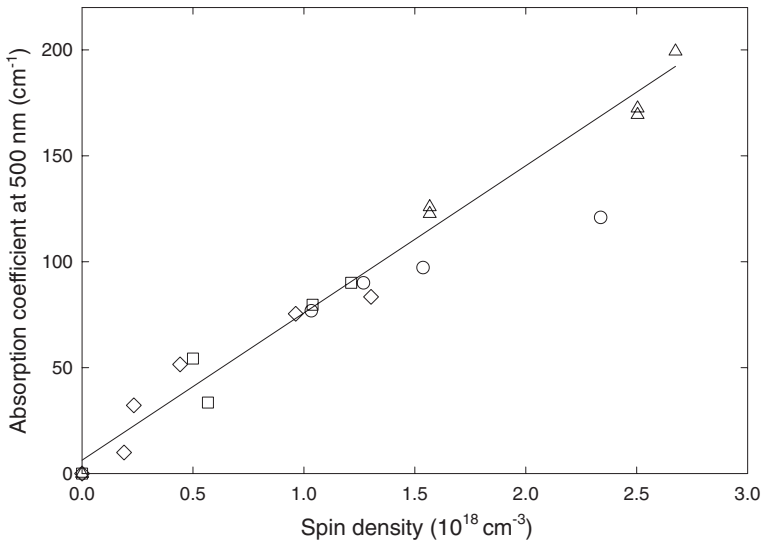

Figure 10. Maximum absorption coefficient at 500 nm versus the volume density of the A-centre for as-received ⟨100⟩ YSZ single crystals implanted with 200 MeV Ni (open circles) and 200 MeV Au ions (open triangles), and as-received ⟨110⟩ YSZ single crystals implanted with 230 MeV Br (open diamonds) and 120 MeV I ions (open squares). The solid line is the least-squares-fitted curve of the Au data.

Least-squares fits of equation (2) to the data give N_∞- and σ-values for the A-centre (table 1). For electron irradiation, similar values are found for the B-centre production ($\sigma = 5.2 \times 10^{-19}$ cm^2, with $N_\infty = 3.5 \times 10^{18}$ cm^{-3}). Cross-section values (σ_o) are also

obtained from the optical absorption growth curves for Ni, Br, I, and Au ions (figure 9) by using the same functional form for the OD at 500 nm versus fluence as in equation (2) with an asymptotic value OD_∞. The σ_o values are in reasonably good agreement with the cross sections deduced from EPR data (table 1). This goes along with the linear relationship between the absorption coefficient at 500 nm and the density of the A-centre (figure 10). A similar broad absorption band centred either at 2.3 or 2.6 eV has already been found with 340 keV Xe-ion-implanted [14] or neutron-irradiated [15] YSZ, respectively.

4.2. Defect creation mechanism

In order to understand the underlying mechanism of defect production, we have calculated the average yield (Y) of A-centre production per ion with respect to the mean number of displaced atoms per ion (N_d) by elastic collisions. Y is defined by

$$Y = N_\infty \sigma x / N_d \tag{4}$$

where $x = R_p$ (the mean projected range) for implanted ions, and $x = h$ (sample thickness) for transmitted ions. The N_d values on both Zr and O sublattices were computed with the TRIM96 [9] simulations using the same displacement energy threshold $E_d = 40$ eV for Zr and O atoms [3]. Y ranges between 2.0 and 4.2% with a mean value near 2.9% for the ⟨100⟩ AR samples, and between 0.6 and 2.5% with a mean value near 1.8% for the ⟨110⟩ AR-samples (table 1). About the same value near 3% is found either for transmitted or implanted 145 MeV C ions, while N_d varies by a factor close to 6. Larger Y-values are found with the R-samples (table 1).

For 2.5 MeV electron irradiations, the number of displaced atoms per electron (N_d) was deduced from the cross section for elastic collisions (σ_d) for the same displacement energy threshold of 40 eV, i.e. $\sigma_d(Zr) = 55$ b and $\sigma_d(O) = 18.5$ b [3]. In this case, N_d is written

$$N_d = [N_a(Zr)\sigma_d(Zr) + N_a(O)\sigma_d(O)]x \tag{5}$$

where $N_a(Zr) = 2.85 \times 10^{22}$ cm^{-3} stands for the atomic volume density of the Zr sublattice and $N_a(O) = 5.70 \times 10^{22}$ cm^{-3} for the O sublattice. Thus Y is written

$$Y = N_\infty \sigma / [N_a(Zr)\sigma_d(Zr) + N_a(O)\sigma_d(O)]. \tag{6}$$

This gives a value of 1.9% in the case of ⟨100⟩ AR samples, which is compatible with the mean yield values found with the ion irradiations. This is in favour of a nuclear collision mechanism of defect production.

We have also calculated the classical radiochemical yield (G), i.e. the number of defects produced per 100 eV of deposited energy:

$$G = 100 N_\infty \sigma x / \Delta E \tag{7}$$

where ΔE is the energy deposited in the electronic excitations expressed in electronvolts. For implanted ions with incident energy E, $\Delta E \approx E$. For transmitted 2.5 MeV electrons the ESTAR code calculation gives $\Delta E = 0.4$ MeV, whereas for transmitted 145 MeV C ions the TRIM96 code calculation gives $\Delta E = 61$ MeV. The G values vary over almost four orders of magnitude (table 1), which rules out a defect production mechanism based on the electronic excitations.

The data of figures 5–6 and 9 are thus reprocessed in a normalized plot of N/N_∞ (or OD/OD_∞) versus the number of displacements per atom (dpas) (figures 11 and 12). For the ions the number of dpas in the Zr and O sublattices is calculated according to the formula

$$\text{dpa} = N_d \phi t / [N_a(Zr) + N_a(O)]x. \tag{8}$$

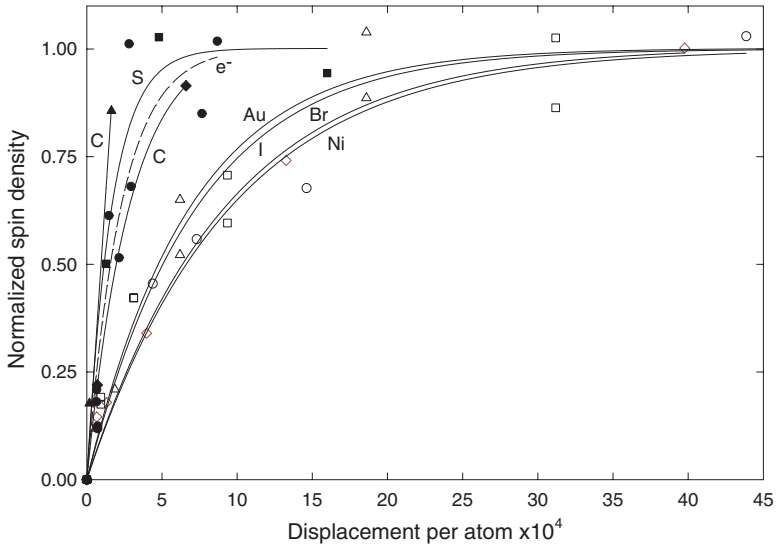

Figure 11. Normalized volume density of A-centre versus number of displacement per atom for as-received ⟨100⟩ YSZ single crystals implanted with 145 MeV C (full diamonds),180 MeV S (full squares), 200 MeV Ni (open circles), 200 MeV I (open squares), and 200 MeV Au ions (open triangles), and irradiated by 2.5 MeV electrons (full circles, dashed curve) and 145 MeV C ions (full triangles), and for as-received ⟨110⟩ YSZ single crystals implanted with 230 MeV Br ions (open diamonds). Lines are least-squares-fitted curves using equation (2).

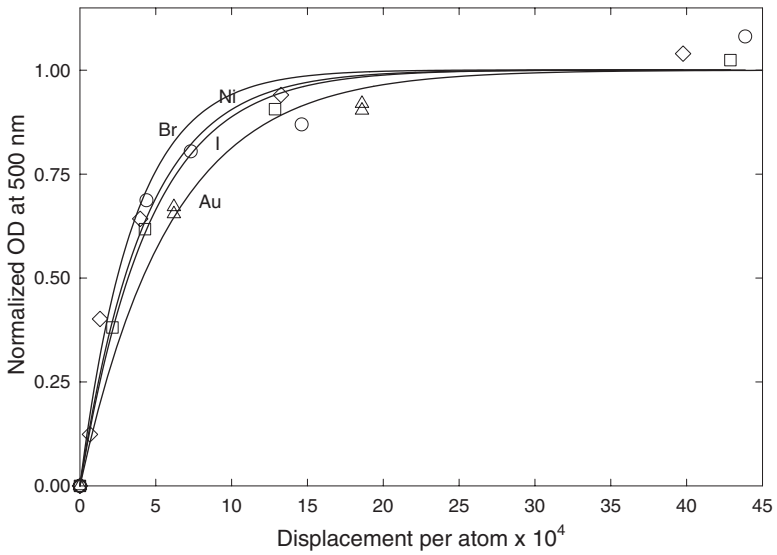

Figure 12. Normalized maximum optical density (at 500 nm) versus number of displacement per atom for as-received ⟨100⟩ YSZ single crystals implanted with 200 MeV Ni (open circles) and 200 MeV Au ions (open triangles), and as-received ⟨110⟩ YSZ single crystals implanted with 230 MeV Br (open diamonds) and 120 MeV I ions (open squares). Solid lines are least-squares-fitted curves using equation (2).

In the case of electrons, it is written

$$\text{dpa} = [\sigma_{\text{d}}(\text{Zr}) + \sigma_{\text{d}}(\text{O})]\phi t. \tag{9}$$

The electron data are rescaled in the same range as the lighter ion (transmitted or implanted C and S) data (figure 11). However, there is a deviation from the heavier ion group (Ni, Br, I, Au) with quite a bit larger N_d-values. In order to reach the same normalized paramagnetic centre density, heavy ions need about twice as many dpas as the electrons and lighter ions. The optical data confirm the good rescaling of the heavier ion data by using the same dpa values (figure 12). No difference is found between the two crystal orientations.

5. Discussion

The main result obtained in this study is that the same two paramagnetic centres are found with heavy ion irradiations as with 2.5 MeV electron irradiations. The same g-factor anisotropies and similar spin–lattice relaxation times for the A-centre are measured in both cases.

The A-centre with an axial ⟨100⟩ symmetry exhibits g-factor values $g_\perp = 1.972$ and $g_\parallel = 1.996$ at RT that are slightly smaller than the free electron value. At low fluences ($\approx 10^{18}$ cm^{-2}), the electron-induced centre was found to anneal out at 450 K [4]. It is thus clearly different from the orthorhombic OHC (O^- centre) with $g_x = 2.019$, $g_y = 2.012$, and $g_z = 2.004$, which is produced by x-ray irradiations at 77 K in YSZ and bleached out at 300 K [5]. It was shown that O^- sits in a C_{2v} symmetry site with one nearest neighbour (NN) Y^{3+} ion [5].

The B-centre exhibits g-factor values $g_\perp = 1.859$ and $g_\parallel = 1.989$ with 2.5 MeV electrons, and $g_\perp = 1.855$ and $g_\parallel = 1.986$ with C ions, which are close to those of the trigonal centre ($g_\perp = 1.852$ and $g_\parallel = 1.989$) or T-centre induced by photon irradiations of YSZ: i.e. one Zr^{3+} ion in a C_{3v} symmetry site with two NN oxygen vacancies along ⟨111⟩ [5–7]. At low fluences ($\approx 10^{18}$ cm^{-2}), the electron-induced centre is bleached at 600 K [4], just like the x-ray-induced one [5]. It is to be noted that these paramagnetic centres cannot be directly associated with impurities since the asymptotic values of the defect density ($N_\infty \approx 10^{17}$–10^{18} cm^{-3}, i.e. ≈5–50 ppm) are much larger than the atomic concentrations of the major transition metal impurities (Ti, ⩽0.5 ppm; Cr, ⩽0.005 ppm; Fe, 0.08 ppm; Ni, ⩽0.005 ppm) measured by GDMS analysis.

On the basis of all these results, the A-centre might be an F^+-type centre, i.e. a singly charged oxygen vacancy with one remaining electron. A small admixture of 3d wavefunctions of NN Zr^{4+} ions into the F^+ ground state could account for the small deviation of the g-values from the free electron value, that should be normally expected for a pure F^+ state with zero angular momentum. This interpretation of the A-centre is consistent with the relatively long spin–lattice relaxation times (figure 3). However, the attribution of the A-centre to a pure F^+-centre cannot explain the axial symmetry of the g-factor with the z-axis along a ⟨100⟩ direction, as each oxygen site of the ZrO_2 lattice exhibits a tetrahedral environment. Substitution of a Zr^{4+} ion by an Y^{3+} should break the tetrahedral symmetry; however, this substitution invariably gives a ⟨111⟩ symmetry. A ⟨100⟩ axial symmetry can be obtained by substituting two Zr^{4+} by two Y^{3+}. However, owing to the 100% abundant nuclear spin $I = 1/2$ of yttrium, we expect a triplet of hyperfine lines with relative intensities 1:2:1 when the magnetic field is parallel to ⟨100⟩, and a more complicated hyperfine pattern for other field orientations. The fact that a single homogeneous (Lorentzian) line is observed for the ⟨100⟩ field orientation implies that the homogeneous line-width is larger than the hyperfine interaction, i.e $A_{hf} < \Delta B_{1/2}/2 \approx 3$ G. This interpretation of the A-centre must be ruled out as long as no residual hyperfine structure is observed.

Another possibility for an axial ⟨100⟩ symmetry of the A-centre involves the localization of the symmetry-breaking defect at an anionic site, at about 2.5 Å from the A-centre position, as only this site is oriented along a ⟨100⟩ direction with respect to the oxygen vacancy. This is probably due to a neutral F-centre, since the density of native oxygen vacancies in YSZ is quite large (≈10 at.%) with respect to the A-centre density.

The assumption of an F^+-type centre is consistent with the production of F-like centres by a nuclear collision mechanism as in oxides such as MgO [16] and α-Al_2O_3 [17] irradiated with 796 MeV Ne and 809 MeV U ions respectively, although these swift ions were in the electronic slowing down regime. It is also in agreement with the correlation between the A-centre and the optical absorption near 2.5 eV (figure 10), seen also in the case of neutron irradiations [15] for which the elastic collisions dominate the damage process. Optical absorption data are rescaled by the dpa values regardless of the heavy ions (figure 12). It is not clear at first sight whether this colour centre is the same defect as the A-centre. However it is important to note that the A-centre is paramagnetic ($S = 1/2$) and that an oxygen vacancy may exhibit two charge states F^+ and F, with spins $1/2$ and 0, respectively. As the F^+ and F absorption bands may be almost superimposed, a good correlation between EPR and optical absorption is expected only if F^+-centres largely dominate the F-centres. The satisfying agreement between EPR and optical absorption (figure 10) indicates that oxygen vacancies are predominantly in the F^+-state.

Since the absorption band shape is not modified when cooling down to 10 K, without apparition of a zero-phonon line, we may conclude that the electron–phonon coupling of this colour centre is quite large. This feature can be accounted for by considering the 4d-Zr admixture into the F^+ ground state, responsible for the small g-shift. Since 4d (t_{2g}) orbitals are mainly non-bonding and 4d (e_g) mainly anti-bonding, a small difference of e_g versus t_{2g} admixture in the ground and excited states of the F^+-centre can shift the excited state potential along the configuration coordinate, with respect to the ground state potential [18]. This results in a strong electron–phonon coupling with a broad absorption band shape.

Figures 11 and 12 show that a correlation exists between the A-centre production and the number of atoms displaced by elastic collisions. It is striking to note that the same paramagnetic defects are found in the case of the dense collision cascades induced by transmitted or implanted heavy ions and in the case of isolated point defects induced by electrons. We thus conclude that the paramagnetic centres are distributed along the damage profile induced by the incident ions and recoiling atoms with a peak near the end-of-range zone, whereas they are homogeneously distributed for electrons. However, more A-centres are created by electrons and lighter ions (C, S) than by heavier ones (Ni, Br, I, Au) for the same displacement damage (figure 11).

The B-centre has an EPR signature similar to that of the photon-induced centre, the so-called T-centre: i.e. one Zr^{3+} ion associated with two oxygen vacancies along $\langle 111 \rangle$ [5–7]. It can thus be produced by the ionization and electronic excitation processes with charged particle irradiations, generating a large number of electron–hole pairs. Zr^{3+} can be formed by the electron capture by Zr^{4+}, while the hole trapped on O^{2-} produces the O^- species unstable at RT. However, this topic would definitely require more reliable data on the defect production kinetics by ion irradiations.

Another unclear point is why no such paramagnetic centres are found at RT in U-ion-implanted AR-samples, whereas they are observed in R-samples. The defect stability is enhanced in the R-samples containing native charge-compensating defects, as was found in our previous results with electron irradiations [3]. It is also important to correlate these results on point defects with the ion-induced stress and strain causing swelling and eventually sample breakage. Further studies will thus involve measurements of the volume expansion in relation to the lattice disorder. Lower-energy electron irradiations are also scheduled in order to scan over the displacement energy threshold of Zr and O atoms.

6. Conclusions

We have studied the defect production in yttria-stabilized zirconia (YSZ) by swift electron and heavy ion irradiations on the basis of EPR and optical absorption spectroscopy data. The same two paramagnetic centres are produced, namely

(i) the A-centre, attributed to an F^+-type centre, i.e. a singly ionized oxygen vacancy, with an axial ⟨100⟩ symmetry, which is induced by the elastic collisions, and
(ii) the B-centre similar to the T-centre, i.e. a Zr^{3+} species associated with two oxygen vacancies along a ⟨111⟩ direction, already found with photon irradiations. The latter defect is probably produced by the electronic excitations deposited in the material by the charged particles.

Acknowledgments

The authors are indebted to Dr S Esnouf (LSI, École Polytechnique, Palaiseau) and Drs J J Grob, J P Stoquert (PHASE Laboratory, Strasbourg), and F Hass (IReS, Strasbourg) for their kind help during the irradiations, and to Ms Yang-Lin Li and Mr B Marcq (LMCP, Paris VI University) for their technical support during the optical absorption spectroscopy measurements.

References

[1] Gong W L, Lutze W and Ewing R C 2000 *J. Nucl. Mater.* **277** 239
[2] Sickafus K E, Matzke Hj, Hartmann Th, Yasuda K, Valdez J A, Chodak P III, Nastasi M and Verall R A 1999 *J. Nucl. Mater.* **274** 66
[3] Costantini J M, Beuneu F, Grynszpan R I and Trautmann C 2002 *Nucl. Instrum. Methods* B **191** 616
[4] Costantini J M and Beuneu F 2002 *Radiat. Eff. Defects Solids* **157** 903
[5] Orera V M, Merino R I, Chen Y, Cases R and Alonso P J 1990 *Phys. Rev.* B **42** 9782
[6] Azzoni C B and Paleari A 1989 *Phys. Rev.* B **40** 6518
[7] Azzoni C B and Paleari A 1991 *Phys. Rev.* B **44** 6858
[8] Ben-Michael R, Tannhauser D S and Genossar J 1991 *Phys. Rev.* B **43** 7395
[9] Biersack J P and Haggmark L G 1980 *Nucl. Instrum. Methods* **174** 257
[10] International Commission on Radiation Units and Measurements (ICRU) 1984 Stopping powers for electrons and positrons *ICRU Report 37* (Bethesda, MD: ICRU) (http://physics.nist.gov/PhysRefData/contents-radi.html)
[11] Castner T G Jr 1959 *Phys. Rev.* **115** 1506
[12] PaiVerneker V R, Petelin A N, Crowne F J and Nagle D C 1989 *Phys. Rev.* B **40** 8555
[13] Wood D L and Nassau K 1982 *Appl. Opt.* **21** 2978
[14] Afanasyev-Charkin I V, Gritsina V T, Cooke D W, Bennett B L and Sickafus K E 2000 *Ceram. Trans.* **107** 535
[15] Savoini B, Cáceres D, Vergara I, Gonzáles R and Muñoz-Santiuste J E 2000 *Nucl. Instrum. Methods* B **277** 199
[16] Pérez A and Thévenard P 1987 *Ion Beam Modification of Insulators* ed P Mazzoldi and G W Arnold (Amsterdam: Elsevier) chapter 4, p 156
[17] Canut B, Benyagoub A, Marest G, Meftah A, Moncoffre N, Ramos S M M, Studer F, Thévenard P and Toulemonde M 1995 *Phys. Rev.* B **51** 12194
[18] Henderson B and Imbush G F 1989 *Optical Spectroscopy of Solids* (Oxford: Oxford Science) chapter 7